J. Fluid Mech. (2013), *vol.* 734, *pp.* 567–594.
doi:10.1017/jfm.2013.486

Experimental evidence of new three-dimensional modes in the wake of a rotating cylinder

A. Radi[1], M. C. Thompson[1,†], A. Rao[1], K. Hourigan[1,2] and J. Sheridan[1]

[1]Fluids Laboratory for Industrial and Aeronautical Research, FLAIR, Department of Mechanical and Aerospace Engineering, Monash University, VIC, 3800, Australia

[2]Division of Biological Engineering, Monash University, VIC, 3800, Australia

(Received 28 February 2013; revised 11 July 2013; accepted 10 September 2013; first published online 14 October 2013)

A recent numerical study by Rao *et al.* (*J. Fluid Mech.*, vol. 717, 2013, pp. 1–29) predicted the existence of several previously unobserved linearly unstable three-dimensional modes in the wake of a spinning cylinder in cross-flow. While linear stability analysis suggests that some of these modes exist for relatively limited ranges of Reynolds numbers and rotation rates, this may not be true for fully developed nonlinear wakes. In the current paper, we present the results of water channel experiments on a rotating cylinder in cross-flow, for Reynolds numbers $200 \leqslant Re \leqslant 275$ and non-dimensional rotation rates $0 \leqslant \alpha \leqslant 2.5$. Using particle image velocimetry and digitally post-processed hydrogen bubble flow visualizations, we confirm the existence of the predicted modes for the first time experimentally. For instance, for $Re = 275$ and a rotation rate of $\alpha = 1.7$, we observe a subharmonic mode, mode C, with a spanwise wavelength of $\lambda_z/d \approx 1.1$. On increasing the rotation rate, two modes with a wavelength of $\lambda_z/d \approx 2$ become unstable in rapid succession, termed modes D and E. Mode D grows on a shedding wake, whereas mode E consists of streamwise vortices on an otherwise steady wake. For $\alpha > 2.2$, a short-wavelength mode F appears localized close to the cylinder surface with $\lambda_z/d \approx 0.5$, which is presumably a manifestation of centrifugal instability. Unlike the other modes, mode F is a travelling wave with a spanwise frequency of $St_{3D} \approx 0.1$. In addition to these new modes, observations on the one-sided shedding process, known as the 'second shedding', are reported for $\alpha = 5.1$. Despite suggestions from the literature, this process seems to be intrinsically three-dimensional. In summary, our experiments confirm the linear predictions by Rao *et al.*, with very good agreement of wavelengths, symmetries and the phase velocity for the travelling mode. Apart from this, these experiments examine the nonlinear saturated state of these modes and explore how the existence of multiple unstable modes can affect the selected final state. Finally, our results establish that several distinct three-dimensional instabilities exist in a relatively confined area on the Re–α parameter map, which could account for their non-detection previously.

Key words: vortex shedding, vortex streets, wakes/jets

† Email address for correspondence: Mark.Thompson@monash.edu

1. Introduction

The flow around a circular cylinder can be considered as a prototype of incompressible bluff body flows. It has been studied for over a century (Bénard 1908; Kármán 1911), and many of its characteristics are well understood. Research has been focused particularly on the wake behind the cylinder, which exhibits a range of interesting phenomena. The wake develops a series of distinct regimes, depending on the Reynolds number $Re = dU/\nu$, with d being the cylinder diameter, U being the free-stream velocity and ν being the kinematic viscosity of the fluid.

Common to all regimes above $Re \approx 46$–49 (Jackson 1987; Dusek, Le Gal & Fraunie 1994; Williamson 1996*c*; Le Gal, Nadim & Thompson 2001; Kumar & Mittal 2006) is the shedding of spanwise vortices of alternate sign from the cylinder surface. Below $Re \approx 190$, these vortices are two-dimensional, and represent what is known as the Bénard–von Kármán vortex street.

For higher Reynolds numbers, this double row of vortices serves as a base flow, on which three-dimensional modes develop. Clearly identified since the work by Williamson (1988), Zhang *et al.* (1995), Barkley & Henderson (1996), Thompson, Hourigan & Sheridan (1996), Wu *et al.* (1996), Henderson (1997) and others, are modes A and B. Both consist of pairs of secondary streamwise vortices, but have different wavelengths and spatiotemporal symmetries. Mode A becomes unstable at $Re \approx 190$ with a spanwise wavelength of $\lambda_z/d = 3$–4 (Williamson 1988; Barkley & Henderson 1996). Its streamwise vortices change sign every shedding period. There is some evidence that this mode is the result of an elliptic instability of the forming Bénard–von Kármán vortex cores (Williamson 1996*b*; Leweke & Williamson 1998*a*; Thompson, Leweke & Williamson 2001). For Reynolds numbers above 220, energy is gradually transferred to mode B, which dominates the wake completely at $Re = 260$ (Williamson 1996*c*). Its vortex pairs have a spanwise spacing of $\lambda_z/d \approx 0.8$, and maintain the same sign in each shedding period.

Besides these two modes, which grow on the natural symmetric wake, a third mode has been observed by several researchers. Mode C was reported by Zhang *et al.* (1995) for $170 < Re < 270$, when a thin control wire was placed close (downstream) to the cylinder surface. The wavelength was $\lambda_z/d = 1.7$ in simulations, and $\lambda_z/d \approx 2$ in experiments. Yildirim, Rindt & van Steenhoven (2013) extended these experiments and demonstrated the period doubling of the main shedding cycle caused by mode C. Sheard, Thompson & Hourigan (2003*b*, 2005*a*) observed a subharmonic mode ($\lambda_z/d = 1.9$) in simulations, and experiments (Sheard *et al.* 2005*b*), in the wake of a torus aligned normal to the direction of flow. Depending on the aspect ratio of the torus, the mode became unstable at a Reynolds number lower than the well-known modes A and B.

Common to these last two examples is the altered spatial symmetry of the base flow. Placing a wire off-centre, close to the cylinder surface, breaks the planar reflective symmetry of the geometry and the spatiotemporal symmetry of the base flow. The latter symmetry corresponds to invariance on evolving the flow for half a period combined with reflection about the centre plane. In the case of flow past a torus, the otherwise infinite cylinder is curved to form a closed ring, which breaks the geometrical reflective symmetry, and this also breaks the spatiotemporal symmetry. Blackburn & Lopez (2003) showed that true subharmonic modes should not occur for flows with the half-period shift/reflection symmetry such as occurs with the circular cylinder wake.

Another way of breaking the flow symmetry is by spinning a circular cylinder about its axis. In this case, the stagnation point is shifted off the streamwise symmetry plane,

and the wake is deflected in the cross-stream direction, creating a lift force (Magnus effect). The non-dimensional rotation rate $\alpha = \Omega d/2U$ becomes the second control parameter besides Re, where Ω is the angular velocity, d is the cylinder diameter and U is the free-stream velocity. Note the scaling is such that the surface speed of the cylinder matches the free-stream flow speed when $\alpha = 1$.

The effect of rotation rate on the two-dimensional base flow has been well-investigated. It is known that the wake-shedding frequency is a function of the rotation rate (Stojković *et al.* 2003), and that shedding activity can be suppressed altogether if the rotation rate is sufficiently high. Vortex-shedding suppression has been demonstrated in two-dimensional computations by Mittal & Kumar (2003) for $Re = 200$, and rotation rates $0 \leqslant \alpha \leqslant 5$. For $\alpha < 1.91$, the Bénard–von Kármán vortex street was observed. For increasing rotation rates, it became narrower, and was deflected in the cross-stream direction. Shedding ceased beyond $\alpha \approx 1.9$, and the wake became steady, developing a closed streamline around the cylinder (Luo, Chew & Duong 2009).

When increasing the rotation rate further, the wake becomes unstable again for a narrow range of rotation rates. Depending on Reynolds number, the wake resumes shedding at $\alpha = 4$–5 (Mittal & Kumar 2003; Stojković *et al.* 2003; El Akoury *et al.* 2008; Kumar, Cantu & Gonzalez 2011), but at a much lower frequency (*second shedding mode* or *mode II*). For these rotation rates, the shed vortices are of the same sign, indicating an underlying physical mechanism different to that of the typical Bénard–von Kármán wake (Pralits, Brandt & Giannetti 2010; Pralits, Giannetti & Brandt 2013).

The described behaviour was confirmed experimentally by Kumar *et al.* (2011), who observed the decay of vortex shedding at $\alpha \approx 1.9$, and its one-sided reappearance at $\alpha \approx 4.4$. We will use aspects of that study for comparison and partial validation of our experimental set-up in § 3.2.

Much less knowledge exists on the three-dimensional aspects of wakes of rotating cylinders in a free stream. For high rotation rates, the flow becomes susceptible to the centrifugal instability, as reported by Mittal (2004) for $Re = 200$ and $\alpha = 5$. Centrifugal instability was observed along the entire cylinder span as a row of closed vortex loops, encircling the cylinder surface. Nevertheless, the wake remained steady for the parameter pair investigated.

For a low rotation rate of $\alpha = 0.5$, El Akoury *et al.* (2008) describe a three-dimensional instability for $Re \geqslant 220$. The structure and wavelength of this mode suggest that it is essentially mode A. The rotation of the cylinder has a stabilizing effect on the flow, increasing the critical Reynolds number of this mode to 220.

The most extensive study on the three-dimensional stability of spinning cylinder wakes was performed by Rao *et al.* (2013*a*). Using linear (for the steady flows) and Floquet (for the periodic flows) stability analyses several new three-dimensional modes were predicted that are distinctly different from the well-known modes A and B. The findings of this numerical study will be discussed in more detail to explain the motivation behind the experiments of the present paper. The present experimental study seeks to confirm the existence of the predicted modes, and to explore their possible interaction in the fully developed nonlinear state. The (Re, α) parameter map of figure 1 will be used to guide the reader through the experimental findings.

Figure 1 shows the core results of Rao *et al.* (2013*a*) in form of neutral stability curves in the (Re, α) parameter map. The map is divided into two regions by the roughly horizontal dashed line through $\alpha \approx 2$. For rotation rates of the lower region,

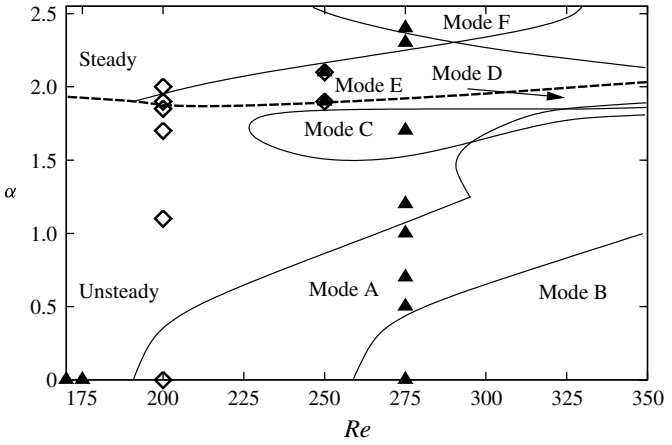

FIGURE 1. Diagram showing the lines of marginal stability in the parameter space for $0 < \alpha < 2.5$ and $170 < Re < 350$. The steady–unsteady transition is marked by a dashed line. The solid lines indicate the marginal stability curves for modes A–F. The points in the α–Re parameter space where experiments were carried out are marked by symbols: empty diamonds for particle image velocimetry and filled triangles for flow visualization, respectively.

the wake resembles the Bénard–von Kármán vortex street with periodic shedding, whereas it is steady for rotation rates above the dividing line.

The three-dimensional transition scenario is similar to that of the non-rotating cylinder for low rotation rates of $\alpha < 1$. The two unstable modes are modes A and B, whose critical Reynolds numbers increase with increasing rotation rates. However, at higher rotation rates of $\alpha > 1$, the three-dimensional scenario becomes increasingly complex, with three new modes identified that bifurcate from the unsteady flow and two modes that bifurcate from the steady flow.

The first new mode, mode C, becomes unstable in a closed region of the (Re, α) plane, centred around $Re = 260$ and $\alpha = 1.7$ (see figure 1). The mode grows with a spanwise wavelength of $\lambda_z/d \approx 1$, and has a purely real but negative Floquet multiplier. This means that this mode is subharmonic, repeating over two cycles of the base flow. We will confirm this property experimentally, yet show that mode C exists also outside of its linearly unstable region, at rotation rates as low as $\alpha = 1$. This surprising observation will be discussed in § 4.1.

Mode D becomes unstable in the narrow region between the top boundary of mode C and the steady–unsteady transition of the two-dimensional base flow, at approximately $\alpha = 1.95$. The mode grows with a characteristic spanwise wavelength of approximately $2d$. When the rotation rate is increased beyond $\alpha = 2$, shedding ceases and the wake becomes steady. Mode D is replaced by mode E, with the wavelength remaining unchanged. Perturbation vorticity plots in Rao *et al.* (2013*a*) show that both modes grow in the region between the highly strained standing vortices in the wake, suggesting the hyperbolic instability as a plausible explanation for both modes. Experimental results on modes D and E will be presented in § 4.3.

Linear stability analysis predicts a second three-dimensional mode on the steady base flow, termed mode F. It grows at higher rotation rates ($\alpha > 2.25$), with a wavelength of $0.45d$. This mode exists primarily in the wall-bounded shear layer of the spinning cylinder, and in the near wake, pointing to a centrifugal instability as

Mode data	C		D		E		F	
	Num.	Exp.	Num.	Exp.	Num.	Exp.	Num.	Exp.
Wavelength [λ_z/d]	1	1.1 (1.8)	2	1.6–1.8	2	2.1	0.45	0.5
Period	$2T$	$2T$	$1T$	$1T$	N/A		0.11^a	0.1^a
Spanwise movement	Stationary		Stationary		Stationary		Travelling	

TABLE 1. Summary of the main characteristics of the newly observed three-dimensional modes C–F. A comparison is made between numerical results (Num.) of Rao *et al.* (2013*a*) and experimental measurements (Exp.) of this publication. (^{a}'period' refers to the period T of the two-dimensional periodic base flow. In the case of mode F, the reference is made to the spanwise movement of the three-dimensional structures, expressed as a Strouhal number St_{3D}.)

its origin (Rao *et al.* 2013*b*). The Floquet multipliers for this mode occur in complex conjugate pairs. This indicates that, while the two-dimensional base flow is steady, transition to this mode marks a transition to three-dimensional flow and the onset of time dependence. This observation will be confirmed by our experimental results presented in § 4.4.

This section has presented only a short overview of the modes described in Rao *et al.* (2013*a*), and we refer the reader to the original paper for an in-depth discussion of mode characteristics and proposed physical mechanisms. For easier comparison with numerical predictions, the (Re, α) map of figure 1 has been annotated with symbols showing the parameter pairs used for the main experiments. A side-to-side comparison of the main characteristics of the newly observed modes is presented in table 1.

2. Experimental set-up and data processing

2.1. *Experimental apparatus*

The experiments were performed in the FLAIR open surface water channel facility. Its test section is 0.6 m wide and 4 m long, with a water depth of 0.77 m. The velocity range is 0.05–0.5 m s^{-1}, with a free stream turbulence level 1–2 % depending on tunnel velocity. The turbulence spectrum is dominated by a streamwise sloshing mode with a frequency of 0.1 Hz. This frequency is at least an order of magnitude smaller than cylinder shedding frequency over the range of tunnel speeds used for these experiments. Filtering out this component results in a background turbulence level of approximately 0.5 %.

As the minimum workable Reynolds number of the tunnel was too high for the desired experiments, an internal structure was built to reduce the tunnel velocity locally within part of the cross-section of the working section. It consists of two parallel transparent acrylic plates (1 m wide, 0.85 m high, 0.36 m apart), which are oriented vertically and in the streamwise direction, a bottom plate, and a perforated screen at the downstream end (see figure 3). The (adjustable porosity) screen creates a pressure drop, which reduces the flow velocity by 40–70 % inside this structure. Effectively, we have built a 'subchannel' inside our main channel test section.

Extensive tests and active design improvements have insured that the flow inside the subchannel is of high quality. The streamwise velocity profiles along the vertical and horizontal directions are uniform within 2 % and 0.5 %, respectively. Overall, the

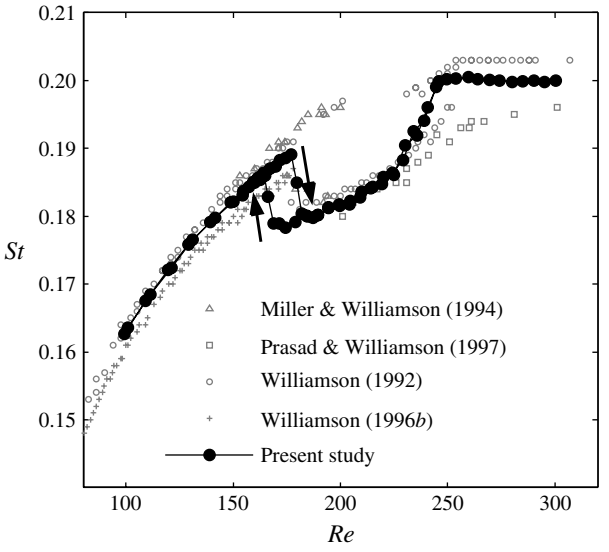

FIGURE 2. For validation of the experimental setup, the shedding frequency of a non-rotating circular cylinder is compared with literature data. The arrows mark the path through the hysteretic discontinuity when increasing (arrow down) and decreasing (arrow up) the Reynolds number.

turbulence intensity and spectrum remain effectively unchanged compared with the main channel. The flow quality was also validated by measuring Strouhal numbers in the wake of a stationary circular cylinder, which were in excellent quantitative agreement with those from the published literature, as can be seen in figure 2. Note that these runs were part of another study, in which suction tubes were employed to manipulate the end conditions as proposed by Miller & Williamson (1994). More details on the construction of the subchannel and all validation tests will be presented in a separate publication.

The rotating cylinder model was mounted vertically in the centre plane of the structure described, positioned one-third downstream of its entrance. The hollow shaft of an archery arrow of 5.82 ± 0.01 mm outer diameter and 800 mm length was used. These arrows are designed for Olympic competition, which effectively guarantees a high degree of straightness and stiffness. The wall material was carbon fibre, with an aluminium mantle and a smooth enamel finish. With a solid blockage of just 1.6 %, no velocity correction was performed on the collected data. The cylinder rotation was driven directly by a stepper motor, whose rotation rate was monitored by an optical encoder.

The end conditions were the channel floor at bottom and the free water surface at top. This resulted in an aspect ratio (cylinder diameter to wetted length) of 130. All coordinates and directions refer to a right-hand Cartesian system, in which the x-axis is aligned with the oncoming flow, the y-axis points in the cross-stream direction and the z-axis coincides with the cylinder axis, pointing upwards.

To quantify its eccentricity of rotation (‘wobbling’), the cylinder was spun in its final configuration outside the water channel and the deflection was measured with a mechanical deflection gauge at several points along its axis. It was found that the deflection distribution is bow-shaped, with minimum deflection amplitudes close to the

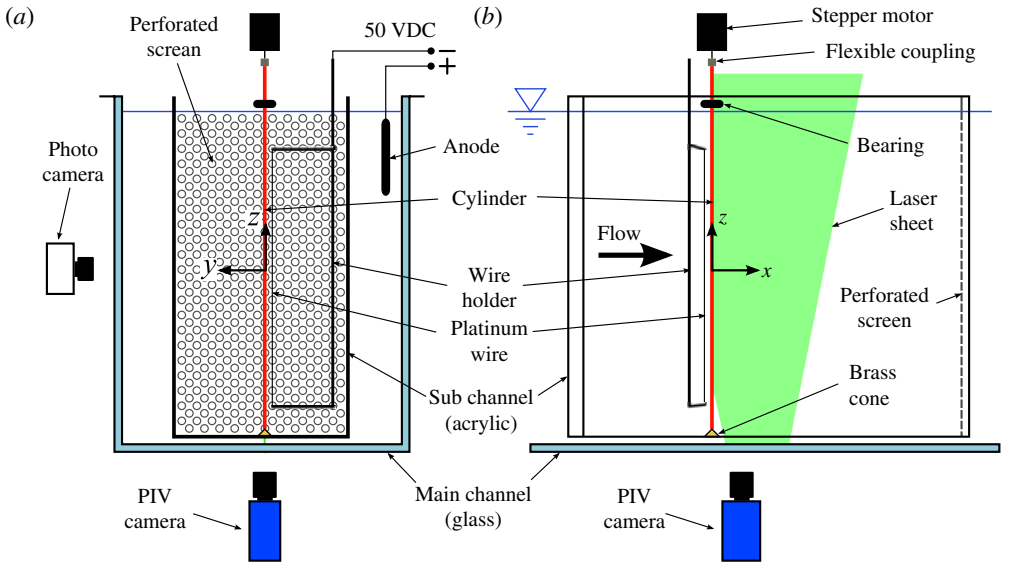

FIGURE 3. (Colour online) Schematic of the setup for the flow visualization experiments. The PIV camera has been included to show its later position: (*a*) view in downstream direction; (*b*) side view. The perforated screen holes are not to scale.

cylinder's two fixed points, and maximum amplitudes at the mid-length of the cylinder. Here, the largest measured half-amplitude was 0.15 mm, equivalent to 2.5 % of the cylinder diameter. Moderate amplitudes of up to 5 % of cylinder diameter can be assumed acceptable, since according to Mittal (2001), who investigated the eccentric cylinder rotation numerically (for $\alpha = 5$), amplitudes between 0.005 and 0.05d did not change the mean flow. Thus, the two-dimensional wake flow can be assumed to be relatively insensitive with respect to disturbances caused by imperfect cylinder rotation.

The maximum deflection due to fluid loading was estimated to be 0.15 mm for the case $\alpha = 5$ at $Re = 200$, using force coefficients from Mittal & Kumar (2003). This deflection is in the same order of magnitude as the bowing due to eccentricity, and is the result of the lift force. The value is highly dependent on rotation rate, and can be expected to be 1/4 of the stated value at $\alpha = 2$.

A 50 μm platinum wire of 500 mm length was positioned upstream, and parallel to the cylinder axis, for hydrogen bubble flow visualizations. The frame that was holding the wire was attached to a tiltable platform (Melles–Griot® kinematic tilt mount 07 MEA 505), which allowed a very accurate alignment of the wire parallel to the cylinder axis. A potential of 50 VDC was sufficient to produce a dense sheet of bubbles. No additional electrolytes were added to the tunnel water. As the water channel was seeded with 10μ particles for particle image velocimetry (PIV) recording, these particles are visible in some flow visualization pictures. The maximum Reynolds number based on the platinum wire diameter was 2.5, meaning steady flow around the wire.

It was observed during the experiments that the best visualization results were achieved when the wire was placed at a certain distance from the x–z symmetry plane. The optimum distance varied with free-stream velocity and rotation rate α,

such that it had to be adjusted for each run. The streamwise location was chosen conservatively with $x/d = -5$, to reduce the risk of a possible interaction between the wire and cylinder wakes. It is known that a thin wire is capable of modifying the wake and forcing new modes, if placed too close to the cylinder (see Zhang *et al.* 1995; Yildirim, Rindt & van Steenhoven 2010).

A continuous laser was used to illuminate the bubble sheet. Shining from below, through the tunnel glass floor, the beam was spread into a sheet of 2–3 mm thickness and aligned parallel to the x–z plane. A Nikon® D7000 camera with 50 mm and 105 mm lenses was used to record still images from a 90° side perspective. In all flow visualizations, the sense of rotation of the cylinder is such that the cylinder surface seen by the observer is moving up. An IDT® Y4 high-speed camera was used for video recordings, operating at a rate of 30–50 frames per second. The data were 8-bit greyscale BMP pictures, which could be directly processed in MATLAB® (see § 2.2).

PIV data were recorded in the x–y plane with a PCO® 4000 camera in double-shutter mode fitted with a 200 mm lens. The camera was mounted under the tunnel, viewing up. The pulsed laser sheet was directed through the tunnel glass wall, perpendicular to the cylinder main axis. An interrogation window size of 32×32 pixels with 50 % overlap resulted in a spatial resolution of 0.35 mm, i.e. $0.06d$. Cross-correlation and vorticity field calculations were performed with an in-house code (Fouras, Lo Jacono & Hourigan 2008).

The free-stream velocity was measured with a laser Doppler velocimetry (LDV) system $15d$ upstream of the cylinder. At this location, the measured value differed by less than 0.5 % for a rotation rate of $\alpha = 5$, compared with a stationary cylinder. The uncertainty of the Reynolds number, Strouhal number and rotation rate was ±3 % at a confidence level of 95 % (for $Re = 200$). This value was dominated by the random error of the velocity measurement, due to the relatively high noise levels of the LDV at such low velocities.

2.2. *Data processing*

Algorithms that were coded in MATLAB® extract information on spatiotemporal symmetry, wavelengths of three-dimensional modes and the Bénard–von Kármán shedding frequency from the recorded flow visualization sequences.

To gain information on spatiotemporal symmetry, space–time (s–t) diagrams were created. In this context an s–t diagram shows the temporal evolution of the flow at a fixed location in space, by plotting some chosen quantity as a function of time. To investigate the temporal behaviour of the three-dimensional modes, we used the brightness distribution in our flow visualization images at a fixed downstream location in the wake. For this purpose, a 10 pixels wide band, parallel to the cylinder axis, was selected at the same downstream location in each picture. This location had to be adjusted for each Reynolds number and rotation rate, to adapt to changes of the flow field. At each point along the span, the band was averaged over its width to form a brightness distribution along the span. The bands of all pictures, plotted as a function of time, formed a space–time diagram.

A windowed ($8d$ wide, 50 % overlap) fast Fourier transform (FFT) was performed on each band of the s–t diagram to calculate the instantaneous spanwise wavelength spectrum. To decrease finite-length effects, a Hamming function was applied to each window. The spectra of all bands were averaged, and the result plotted as a function of wavelength λ_z. The highest peak (besides possible long-wavelength noise) was considered as the mode's spanwise wavelength.

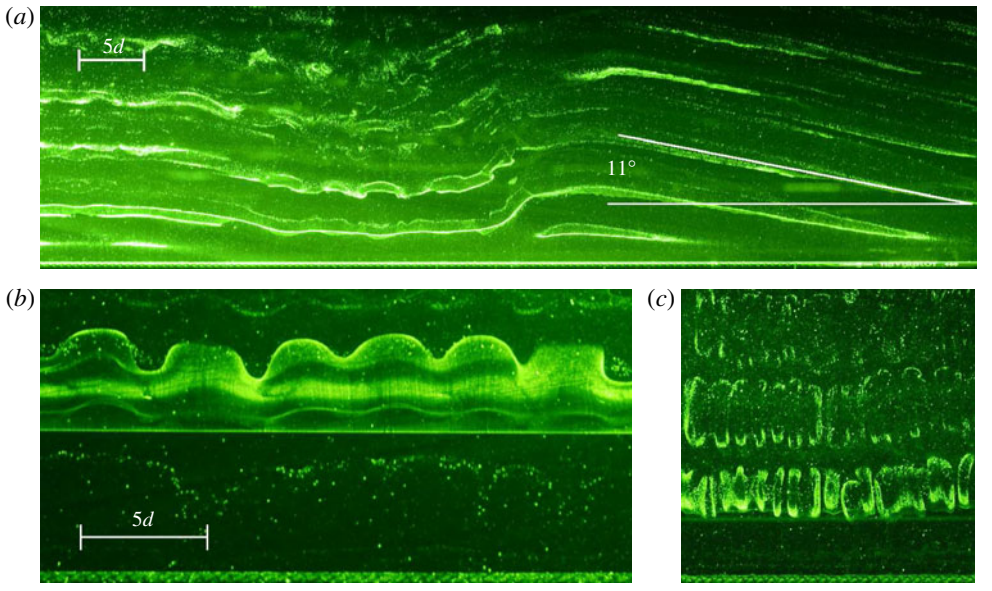

FIGURE 4. (Colour online) Hydrogen bubble flow visualizations of the non-rotating cylinder wake: (*a*) oblique shedding on the right is observed simultaneously with a section of developing mode A in the left half of the picture at $Re = 170$. (*b*) Mode A at $Re = 175$, with a spanwise wavelength of $\lambda_z/d \approx 3.4$. The platinum wire is placed at $6.5d$ downstream of the cylinder. (*c*) Mode B at $Re = 275$. The average spanwise wavelength is $\lambda_z/d \approx 0.96$. The platinum wire is not visible in (*a*) and (*c*), being 5 cylinder diameters upstream of the cylinder. The scaling is the same for (*b*,*c*). The cylinder can be seen at the bottom edge of all pictures. The flow is from the bottom up.

To estimate the Strouhal number St of the two-dimensional base flow, a (windowed) FFT in time was performed on all averaged bands. The resulting spectra typically showed a clear peak at the Bénard–von Kármán shedding frequency. A Gaussian normal distribution was fitted on this peak to improve the spectral resolution. The shedding frequency was defined as the mean of the Gaussian fit; the standard deviation could be used as an estimate of the peak width.

3. Validation of the set-up

The current experimental set-up was validated by comparing results of two experiments to published data. First, a flow visualization study was undertaken for the case of a non-spinning cylinder ($\alpha = 0$) to estimate the critical Reynolds numbers and to measure the characteristics of the well known modes A and B (Williamson 1988; Barkley & Henderson 1996). Second, the process of vortex shedding suppression was compared to PIV data of Kumar *et al.* (2011).

3.1. *Non-rotating cylinder*

A two-dimensional Bénard–von Kármán vortex street was observed for Reynolds numbers up to $Re = 160$. Most of the time, the vortices were shed under an angle of up to 12° with respect to the cylinder axis (*oblique shedding*), a value which varied with time and along the spanwise direction (figure 4*a*). This is not surprising, as only careful manipulation of the cylinder end conditions can assure

parallel shedding (see Williamson 1996*b*). For higher Reynolds numbers, irregularities and deformations of the shed vortices appeared (*vortex dislocations*; see Williamson 1996*a*). At $Re \approx 175$, the wake developed a fully three-dimensional character, known as mode A (Williamson 1988). Stability analysis predicts the critical Reynolds number to be approximately 190 (Barkley & Henderson 1996); however, the transition is hysteretic and finite-amplitude perturbations can cause premature onset for Reynolds numbers down to approximately 180 (Henderson 1997). Visualization of this mode in our water channel with the technique employed turned out to be challenging, and the hydrogen bubble wire had to be placed in the wake to provide the picture seen in figure 4(*b*). The wavelength of the spanwise modulations in this image is $\lambda_z/d \approx 3.4$. The preferred wavelength from Floquet stability analysis is $3.96d$, although the mode is unstable over a reasonably wide wavelength band (Barkley & Henderson 1996).

For Reynolds numbers above 200, mode B developed gradually and dominated the wake for $Re > 270$, in good agreement with the careful experiments of Williamson (1996*b*). Figure 4(*c*) shows a flow visualization at $Re = 275$. Streamwise vortices of mode B are clearly distinguishable. Numerical processing of a sequence of 1000 pictures, as described in § 2.2, gives an average spanwise wavelength of $\lambda_z/d \approx 0.96$. Floquet analysis predicts the most unstable wavelength as $0.822d$ (Barkley & Henderson 1996). The Strouhal number is $St = 0.194$, in good agreement with values found in the literature (e.g. $St \approx 0.202$ in Norberg (1987)).

3.2. *Rotating cylinder*

PIV data were recorded to validate our setup for the case of a rotating cylinder. Six rotation rates between $\alpha = 0$ and $\alpha = 2.0$ were chosen at $Re = 200$. For rotation rates above $\alpha \approx 2$ and Reynolds numbers above 100, the Bénard–von Kármán vortex street can be fully suppressed, resulting in a steady laminar double shear layer wake. This unsteady to steady transition region is marked by the dashed line in figure 1.

Kumar *et al.* (2011) demonstrated this phenomenon experimentally for Reynolds numbers $Re = 200$–400, and rotation rates $0 < \alpha \leqslant 2.1$. Their figure 6 shows the decay of vortex shedding at $\alpha \approx 1.95$ for $Re = 200$. We repeated these experiments, and our results are shown in figure 5; the same flow behaviour was observed. The flow resembled the typical Bénard–von Kármán vortex street for low values of α. For increasing rotation rates, the double-row of vortices was deflected in cross-stream direction. At the same time, the shedding became weaker, as indicated by the decreased peak vorticity values. For $\alpha = 1.85$, the vortices were highly stretched, and the wake resembled a snake-like pattern. For $\alpha = 1.90$, shedding ceased completely, and the steady wake consisted of the merger of the two separated shear layers. This wake showed some intermittent 'flapping', probably due to slight variations of free stream velocity. This rotation rate marks the critical value separating the shedding and non-shedding regimes. For all of the higher rotation rates investigated at this Reynolds number, $1.9 < \alpha \leqslant 2.10$, the wake remained steady.

Compared with experiments by Kumar *et al.* (2011), the restabilization happened in our case at a slightly lower value of $\alpha = 1.9$. However, this is consistent with the linear stability analysis by Rao *et al.* (2013*a*), and two-dimensional simulations by Mittal & Kumar (2003), which estimate the critical value to be $\alpha = 1.91$.

In summary, these results show the reliability of our set-up. As a result of the novel modification of our water channel, we were able to reproduce several established flow phenomena of stationary and rotating cylinders. In the following sections, the results of our main experiments are presented, which investigate the structure of newly observed three-dimensional wake instabilities.

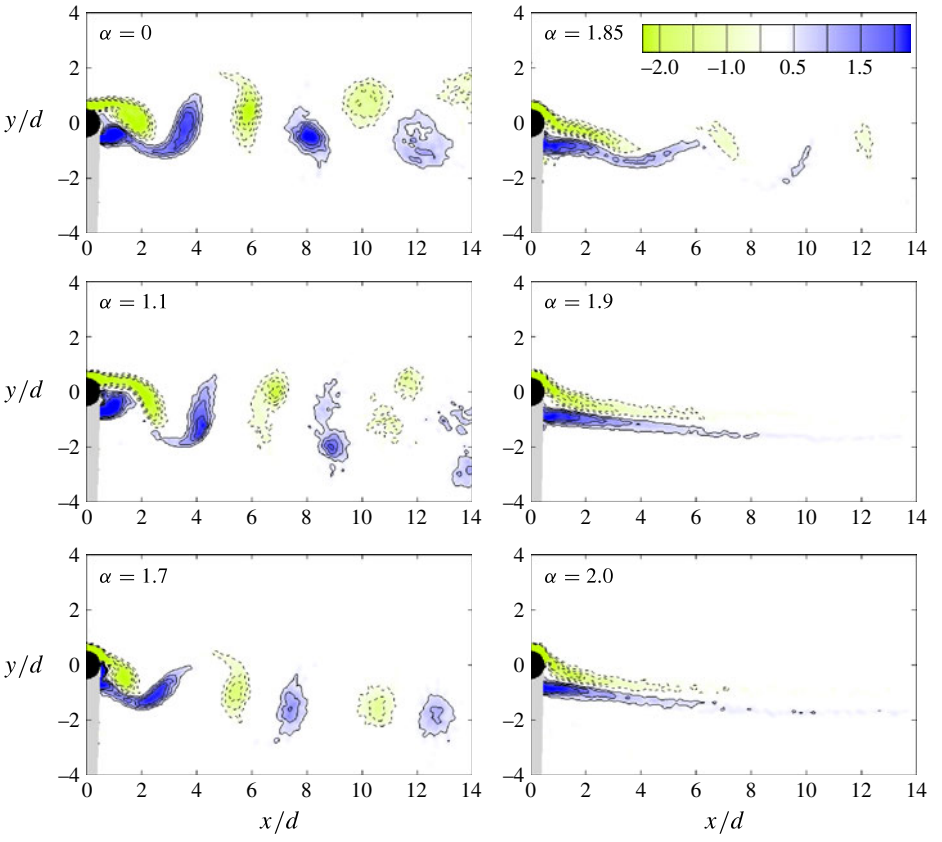

FIGURE 5. (Colour online) Instantaneous PIV vorticity fields in the x–y plane at $Re = 200$ for the marked clockwise rotation rates. Vorticity is non-dimensionalized as $\omega_z d/U$, with solid lines representing positive values. Vortex suppression is observed beyond $\alpha \approx 1.9$. This figure should be compared directly with figure 6 of Kumar *et al.* (2011). The grey areas mask spurious vectors in the obstructed region of the laser sheet.

4. Results and discussion

The main experiments consisted of flow visualizations at $Re = 250$ and $Re = 275$, with subsequent numerical analysis of the digital images. For rotation rates $0 \leqslant \alpha < 2.5$, all modes predicted by the linear stability analysis of Rao *et al.* (2013*a*) were observed. In addition to the well-known mode B for $\alpha = 0$, these were: the subharmonic mode C; mode D and its non-shedding version mode E; and for rotation rates above $\alpha = 2.3$, a short-wavelength mode F on the cylinder surface. The modes differ in their wavelengths, spatiotemporal symmetries and underlying base flows. Evidence will be presented of mode F being a travelling wave mode. See table 1 for a comparison of mode properties between the linear stability analysis predictions and experimental measurements.

4.1. *Mode C*

Mode C is described for $Re = 275$ and $\alpha = 1.7$. As seen in figure 1, this parameter combination lies in the centre of the region of the parameter space occupied by this linearly unstable mode. Here, the linear amplification rates can be expected to

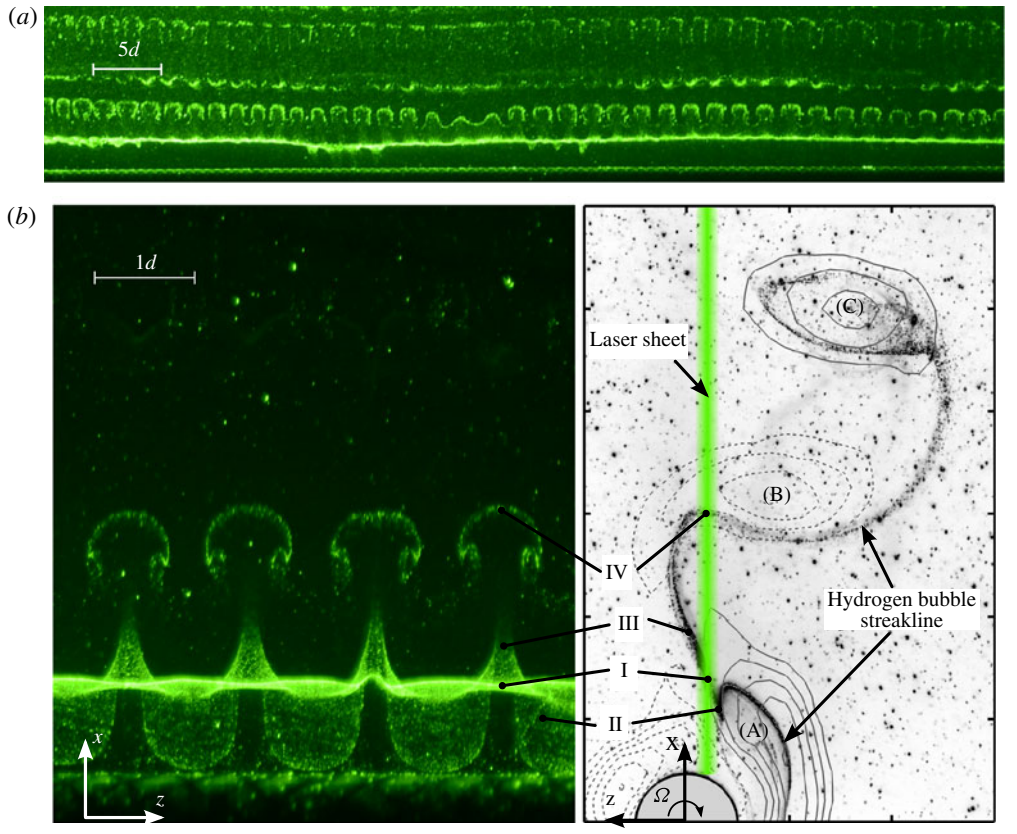

FIGURE 6. (Colour online) The subharmonic mode C at $Re = 275$. (*a*) Large-field view of the wake ($70d \times 12d$), showing the strict spanwise periodicity at $\alpha = 1.2$. (*b*) Close-up view of the near wake at $\alpha = 1.7$: a row of streamwise double vortices is shown in the flow visualization on the left, and the corresponding wake cross-section is seen on the right (both views are to scale). In the picture on the right, instantaneous vorticity contours are overlaid on the PIV snapshot. The hydrogen bubbles create the dark streakline. The flow is from the bottom to the top.

be highest, which should make the detection of this mode in experiments easier. Nonetheless, the visibility of this mode was very dependent on the correct positioning of the hydrogen bubble wire. Cross-stream movements of the wire of ± 1 mm made this mode invisible and created the impression of only slightly disturbed two-dimensional laminar shedding. Once the correct wire location was found, the mode could be visualized reliably for a wide range of rotation rates. However, this difficulty in detection is an indication that the saturated state of the mode does not lead to strong distortion of the otherwise two-dimensional nature of the wake, at least at this Reynolds number.

Figure 6(*a*) shows the strict periodicity of mode C along a span of $70d$. The flow structures will be described with the help of the close-up views in figure 6(*b*). The photograph on the left is a flow visualization in the x–z plane similar to figure 6(*a*), whereas the picture on the right shows the wake cross-section in the x–y plane. The latter picture shows the first frame of a PIV double exposure (inverse colour), overlaid with ω_z-vorticity contours calculated for this vector field. The non-dimensional contour

levels range from -3 to $+2.5$ excluding 0, in steps of ± 0.5, with solid lines denoting positive vorticity. The hydrogen bubble wire upstream of the cylinder was switched on during the recording, such that the bubble sheet cross-section can be seen as a dark streakline. The black speckles are PIV seeding particles. The two views in figure 6(*b*) were not recorded simultaneously, but represent the same stage of the shedding cycle. The approximate location of the laser sheet used for flow-visualization is marked in the picture on the right.

The flow visualization on the left (and similarly in figure 6*a*) can be interpreted the following way: the bubble sheet passes the rotating cylinder on the side facing away from the observer. The bubbles enter the near wake and cross the laser sheet at the location marked by I. The bubble sheet moves out of the plane of the paper where it is illuminated and creates the bright wavy line. Approximately at this location the sheet splits up into a section that is moving upstream (marked as II) and is being wrapped around the forming vortex core (A), and a section that is moving downstream (III). Already at this stage, the bubble sheet is deformed with a periodic spanwise modulation. The upstream-moving part consists of a series of U shapes, where the missing sections have been 'folded out', and move in the downstream direction. These sections form the stems (III) leading to the mushroom shapes at IV. These shapes are typically created by a row of counter rotating double vortices. The laser sheet cuts through these streamwise vortices at IV.

It is evident that sections III experience strong stretching between the forming vortex (A) and the downstream moving vortex (B), which leads to amplification of streamwise vorticity. Furthermore, it is suggested that the bubble sheet entrains the near wake in the vicinity of an instantaneous saddle point (Délery 2001), close to marker I. This would explain the splitting of the sheet into upstream and downstream moving sections. These observations lead to the conclusion that the mode C instability develops within 1–2 cylinder diameters downstream of the cylinder, its streamwise double vortices reside in the braid region and get amplified through stretching of this braid region between consecutive Bénard–von Kármán vortices.

To investigate the temporal development of mode C, space–time diagrams have been created using the technique described in § 2.2. Figure 7(*a*) shows a space–time diagram at $Re = 275$ and $\alpha = 1.7$, created from pixel data at $x/d = 3$. At this location, the streamwise vortices are visible as mushroom shapes. The subharmonic nature of mode C can be inferred from the arrangement of these patterns, each of which is repeated every second shedding cycle. Equivalently, every 'valley' of the pattern is aligned with a 'peak' of the successive shedding cycle.

Figure 7(*b*) shows the spanwise wavelength spectrum, created by performing an FFT analysis of the space–time diagram. The peak shows the dominant spanwise wavelength of $\lambda_z/d = 1.1$. A small side peak can be seen at the first higher harmonic (half the wavelength), and the spectral power rises again for larger wavelengths due to larger-scale spanwise irregularities of the wake.

4.2. *Co-existence of modes B and C*

The wake of a stationary cylinder ($\alpha = 0$) at $Re = 275$ exhibits an (almost) pure mode B wake. A rotating cylinder at the same Reynolds number, but at $\alpha = 1.7$, leads to pure mode C, as shown in the previous section. It follows that a transition from one mode to the other has to take place somewhere between these two rotation rates. According to the neutral stability curves in figure 1, the following observations should be expected: mode C is linearly unstable only above the critical rotation rate $\alpha_{crit} \approx 1.5$; for slightly lower rotation rates, the wake should exhibit purely two-

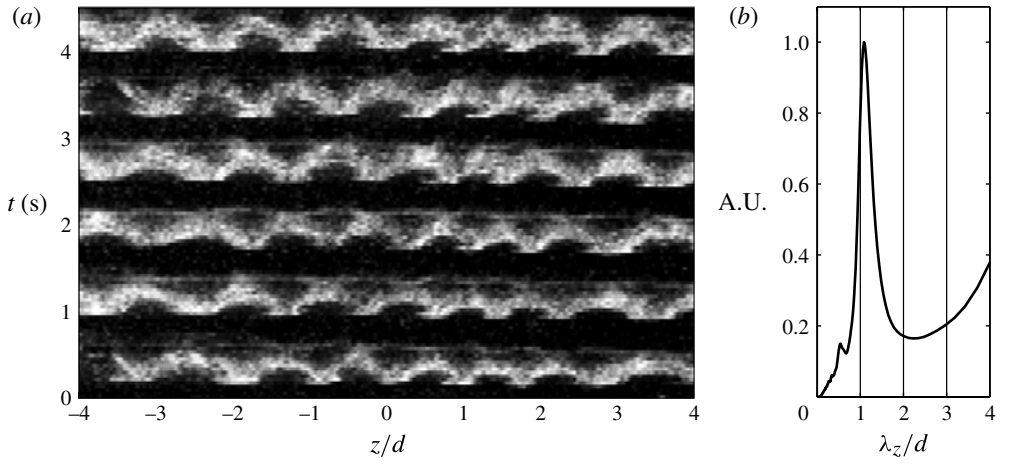

FIGURE 7. (*a*) Space–time diagram at $x/d = 3$ and (*b*) time-averaged spanwise wavelength spectrum of mode C at $Re = 275$ and $\alpha = 1.7$. The dominant spanwise wavelength is represented by the peak in the spectrum at $\lambda_z/d \approx 1.1$. The subharmonic nature of mode C is revealed in (*a*) by the interchange of peaks and valleys every shedding period.

dimensional shedding; for rotation rates $\alpha \lesssim 1.1$, mode A becomes unstable, before mode B develops for $\alpha \lesssim 0.5$. It will be tested whether this rather complex transition scenario really takes place in the experiment.

The same type of experiments as in the previous section (flow visualizations, with subsequent numerical analysis) were performed for $0 < \alpha \leqslant 1.7$, at $Re = 275$. In contrast to the scenario outlined above, mode C was found to dominate the wake for rotation rates far below $\alpha_{crit} \approx 1.5$. Its flow structures and subharmonic nature were observed at $\alpha = 1.0$, and traces remained visible even at $\alpha = 0.7$. Unlike the linear prediction, the wake never lost its three-dimensionality, meaning that no purely two-dimensional shedding was observed. In addition, no traces of mode A could be found in flow visualizations for $0.5 \lesssim \alpha \lesssim 1.1$.

The spanwise wavelength of mode C was found to be dependent on the rotation rate. Figure 8(*a*) shows that in the linearly unstable region (to the right of the dashed vertical line), the wavelength was $\lambda_z/d \approx 1.1$, in good agreement with predictions by Rao *et al.* (2013*a*). For rotation rates below $\alpha_{crit} \approx 1.5$, the wavelength of mode C increased steadily as α was decreased, and almost doubled for $\alpha = 0.5$ (round symbols). For rotation rates below $\alpha \approx 1.0$, the flow became increasingly irregular. Neither the wavelength, nor the subharmonic nature of mode C could be clearly observed. The three-dimensional flow patterns were changing randomly with time, and lacked spatial coherence. This leads us to conclude, that this marked the practical transition from mode C to B.

Some chosen wavelength spectra are shown in figure 8(*b*) for a series of rotation rates. The identified peaks of mode B and C are marked by round and square symbols, consistently with figure 8(*a*). The smaller second peaks at $\alpha = 1.0$ and 1.5 are higher harmonics, caused by a slight square wave appearance of the flow structures moving through the sampling region in the flow visualization pictures. The origin of the smaller peak at $\alpha = 0.7$ is ambiguous, as the flow has lost its spanwise periodicity at this rotation rate. It can likely be attributed to mode B, as structures with this wavelength are intermittently present in the flow visualizations.

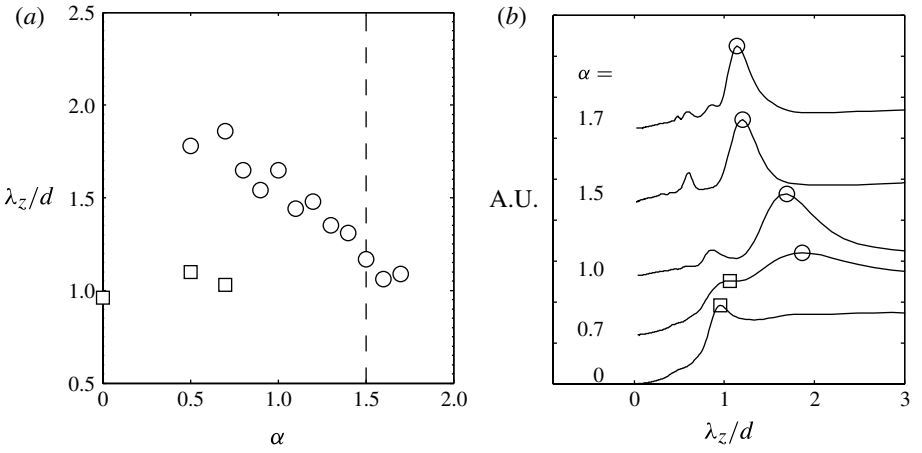

FIGURE 8. Co-existence of modes B and C at $Re = 275$ is shown in terms of spanwise wavelengths. (*a*) Wavelength as function of rotation rate. Circular symbols depict mode C, square symbols are associated with mode B. To the right of the dashed vertical line, mode C is linearly unstable, according to Rao *et al.* (2013*a*). (*b*) Wavelengths spectra for chosen rotation rates show a gradual transition to mode C for increasing α. The spectra are shifted with respect to each other in vertical direction for clarity. The spectra are based on measurements at $x/d = 3$–5, depending on α.

The spectra of figure 8(*b*) can be interpreted as follows. Mode B exists in a spanwise incoherent flow ($\alpha = 0$). Its peak is small, and hardly dominates the long-wavelength background noise that is the plateau at $\lambda_z/d > 1$. Out of this noise, the peak of mode C rises, when α is increased. For very small rotation rates, it is centred around a wavelength of two cylinder diameters, but shifts to lower wavelengths as α is increased, reaching its terminal value of $\lambda_z/d \approx 1.1$ at $\alpha \geqslant 1.5$. Throughout this process, the peak becomes narrower and higher, soon dominating the background noise. This is caused by the flow becoming more coherent in the spanwise direction; the flow reaches a high degree of regularity already at $\alpha = 1.0$.

To support the conclusions drawn from the wavelength spectra, figure 9 shows mode C flow structures at $\alpha = 0.7$ and 1.7. At the lower rotation rate, the spanwise wavelength is $\lambda_z/d \approx 1.8$, whereas at the higher rotation rate, the wavelength decreases to $\lambda_z/d \approx 1.1$, consistent with the linear predictions by Rao *et al.* (2013*a*).

One should bear in mind that the wavelength spectra are a statistical representation of the flow. They have been extracted from flow visualizations that depend on the position of the hydrogen bubble wire and the laser sheet. In addition, the streamwise location in the pictures from which the wavelength spectra were created, influenced, to some degree, the relative strengths of the two peaks representing modes B and C. In this sense, the data of figure 8 should be treated as a rough sketch of the transition process between these two modes. A more robust experimental technique is needed to investigate this transitional region in more detail.

The observation of mode C below the critical rotation rate of $\alpha_{crit} \approx 1.5$, stands out as the greatest difference between linear stability analysis and experiment. An explanation for this unexpected behaviour might be the initial conditions in the experiments. Each point on the parameter map was approached from $\alpha = 0$, by quickly spinning up the cylinder from rest. This way, the initial condition at $Re = 275$ was a fully developed mode B. Within a few seconds, the cylinder was spinning at its

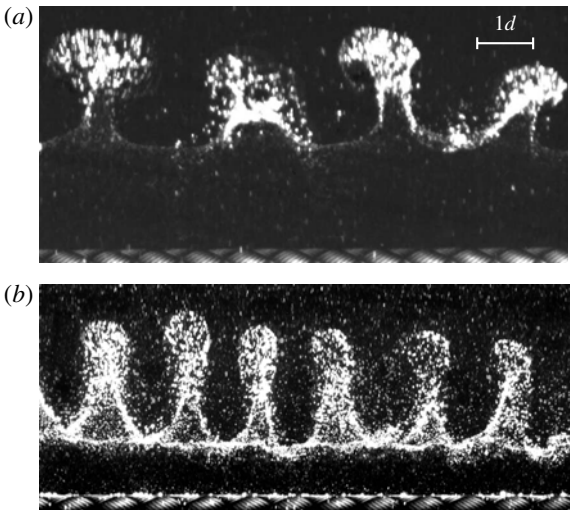

FIGURE 9. Change of wavelength of mode C with rotation rate at $Re = 275$. (*a*) The average wavelength is $\lambda_z/d \approx 1.8$ at $\alpha = 0.7$. (*b*) The wavelength decreases to $\lambda_z/d \approx 1.1$ at $\alpha = 1.7$. Each picture is $7d$ wide.

terminal rotation rate, and any new mode would have to grow on this base flow. This excludes a possible hysteresis effect of mode C, which may have been observed if the rotation rate was changed continuously. Instead, it is speculated that the presence of mode B triggers mode C, forcing it outside its predicted instability region to lower values of α.

A similar relationship exists between modes A and B of a stationary cylinder. Mode A becomes linearly unstable through a subcritical bifurcation at $Re \approx 190$ (Henderson 1997). The critical Reynolds number for the onset of linear instability of mode B is $Re \approx 260$. This number is derived assuming a purely two-dimensional base flow. In spite of this, mode B has been experimentally and numerically observed by many researchers for Reynolds numbers below this critical value, some of them as low as $Re = 220$ (Williamson 1988; Zhang *et al.* 1995; Thompson *et al.* 1996). Henderson (1997) and Barkley, Tuckerman & Golubitsky (2000) explain this observation by a nonlinear interaction of these modes, in which mode A has a destabilizing effect on mode B, and mode B has a stabilizing effect on mode A, with a resulting mixed-mode state emerging from $Re \approx 230$ on. Sheard, Thompson & Hourigan (2003*a*) extended this further using a coupled Landau model again showing that in practice the transition from mode A to mode B occurs over the Reynolds number range $230 \leqslant Re \leqslant 260$. Remarkably, once the Reynolds number exceeds the critical value of $Re \approx 260$, this mixed-mode state gives way to what appears to be a much more 'pure' mode B wake.

A similar nonlinear interaction may be at play at the transition of mode B to C, with rotation rate α as the control parameter. Confirmation of this conjecture, and the general influence of initial conditions on mode C, need further investigation.

4.3. *Modes D and E*

Once the rotation rate was increased above $\alpha \approx 1.85$, two new modes, termed here as modes D and E, develop in rapid succession on further increasing the rotation rate. As they have very similar characteristics, both modes will be discussed in this section.

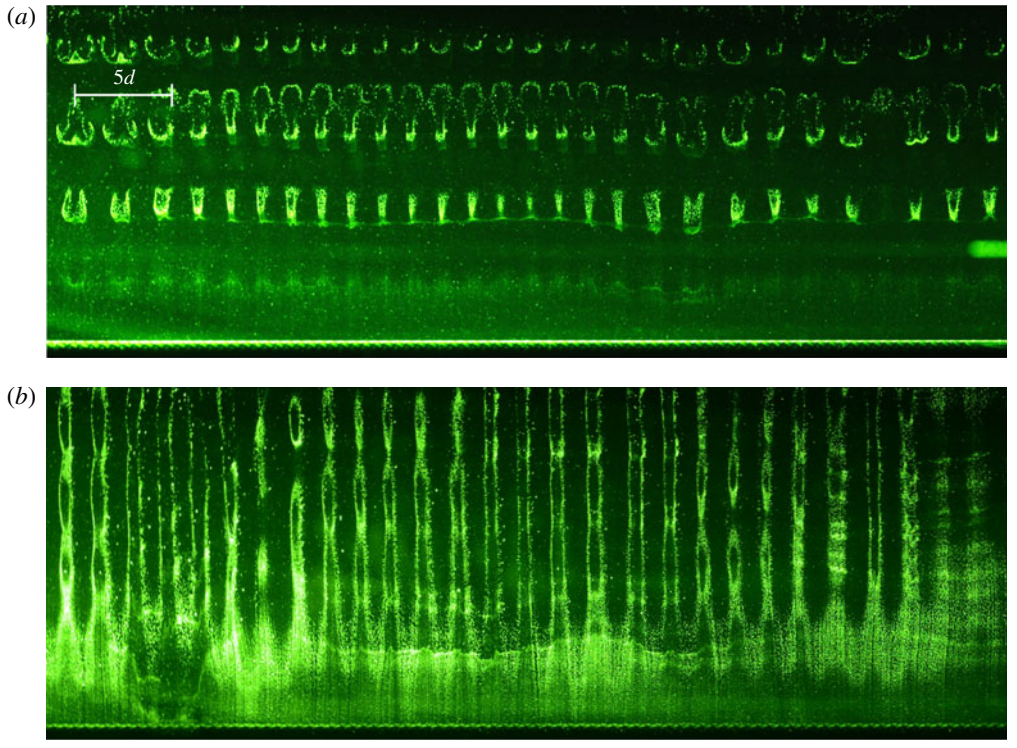

FIGURE 10. (Colour online) Flow visualizations of (*a*) mode D and (*b*) mode E at $Re = 250$, $\alpha = 1.9$ and $\alpha = 2.1$, respectively. The flow is from bottom up.

Note that the following experiments were performed at a slightly lower Reynolds number of $Re = 250$.

Linear stability analysis predicts mode D to exist for a narrow band of rotation rates, approximately $1.85 < \alpha < 1.95$. At these rotation rates, the cylinder wake is on the verge of undergoing transition from a shedding state to a laminar steady double-shear layer wake, as discussed previously in § 3.2. Mode D consists of uninterrupted streamwise vortices that wind around the (now weakened) Bénard–von Kármán vortices, resembling a serpentine pattern. Figure 10(*a*) shows a plan view of this wake at $\alpha = 1.9$. The hydrogen bubble sheet is wrapped around the streamwise vortices of mode D, and becomes illuminated when these cross the laser sheet. The streamwise distance of the illuminated sections in this image is dictated by the separation of the Bénard–von Kármán vortices.

Figure 10(*b*) shows the wake at a slightly higher rotation rate of $\alpha = 2.1$, for which the two-dimensional Bénard–von Kármán shedding no longer occurs. Superimposed on this steady wake, steady streamwise vortices can be seen, with a spanwise spacing similar to that of mode D. Owing to the different base flow, this mode is referred to as mode E.

The temporal behaviour of both modes can be seen in the space–time diagrams of figure 11. Figure 11(*a*) shows that mode D is periodic in time (with $St = 0.206$) and space. Mode E is periodic in the spanwise direction, but steady in time, exhibiting only slight variations due to a small amount of unsteadiness of the wake. In particular, the diamond shaped cells connecting the vertical traces in figure 11(*c*) are formed by

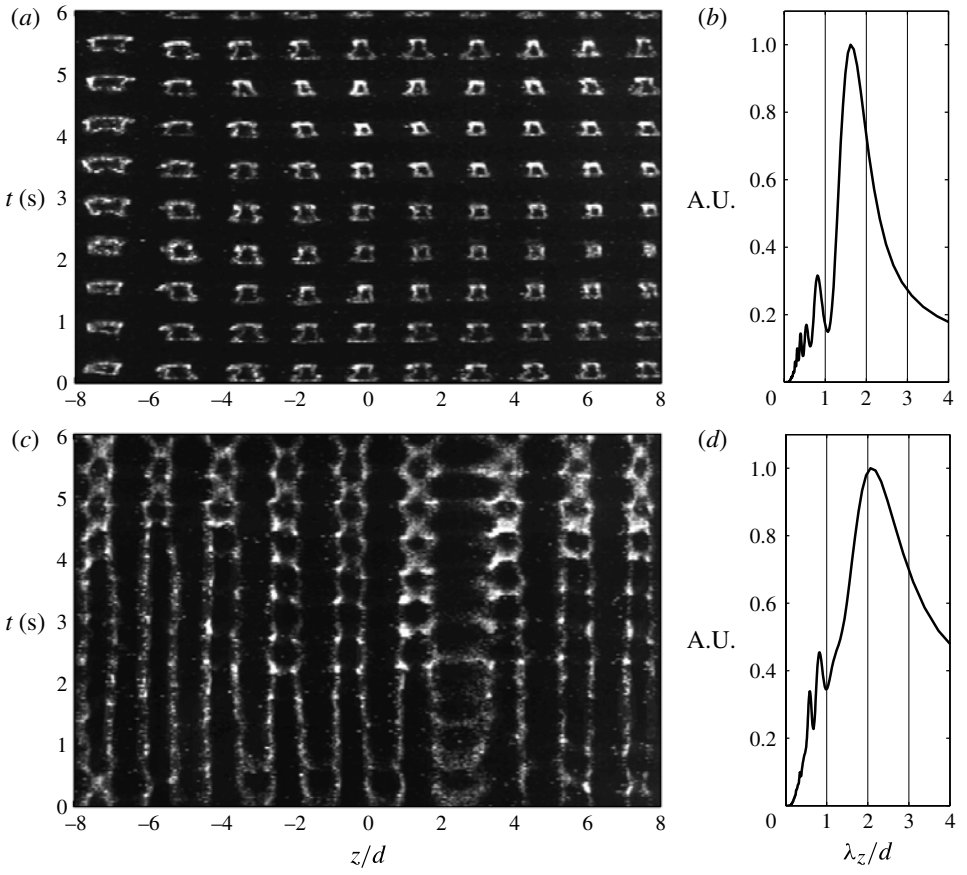

FIGURE 11. Space–time diagrams of (*a*) mode D at $\alpha = 1.9$; and (*c*) mode E at $\alpha = 2.1$ (both created at $x/d = 9.2$). The time-averaged wavelengths are $\lambda_z/d \approx 1.7$ and $\lambda_z/d \approx 2.1$, as seen in wavelength spectra (*b*,*d*), respectively.

a remnant shedding oscillation of the double-shear layer. The reason for the changing linking between the longitudinal vortices at $0 < z/d < 4$ is not clear, but is probably caused by a slight flow disturbance.

The spanwise wavelengths are $\lambda_z/d = 1.7$ for mode D, and $\lambda_z/d = 2.1$ for mode E, as can be seen in the wavelength spectra of figure 11(*b*,*d*). It must be emphasized that these values are an average over the measured space and time domains. The space–time diagrams of figure 11 show only a small spanwise section of the collected data, and also for a particular time window. Particularly for mode D, the full data set shows a slow change in wavelength, which decreases from $\lambda_z/d = 1.8$ to 1.6 over a time period of 45 s (68 shedding periods).

One concern regarding the use of qualitative flow visualization over extended streamwise domains, as in case of modes D and E (figure 10), is the streakline effect with its spatially integrated view of the flow patterns. Combined with vortex stretching and the slow diffusion of the hydrogen bubbles as a passive scalar (Smits & Lim 2000, chap. 3.5), this effect can lead to an misinterpretation of the existence and strength of vorticity (this is shown impressively in Cimbala, Nagib & Roshko (1988)).

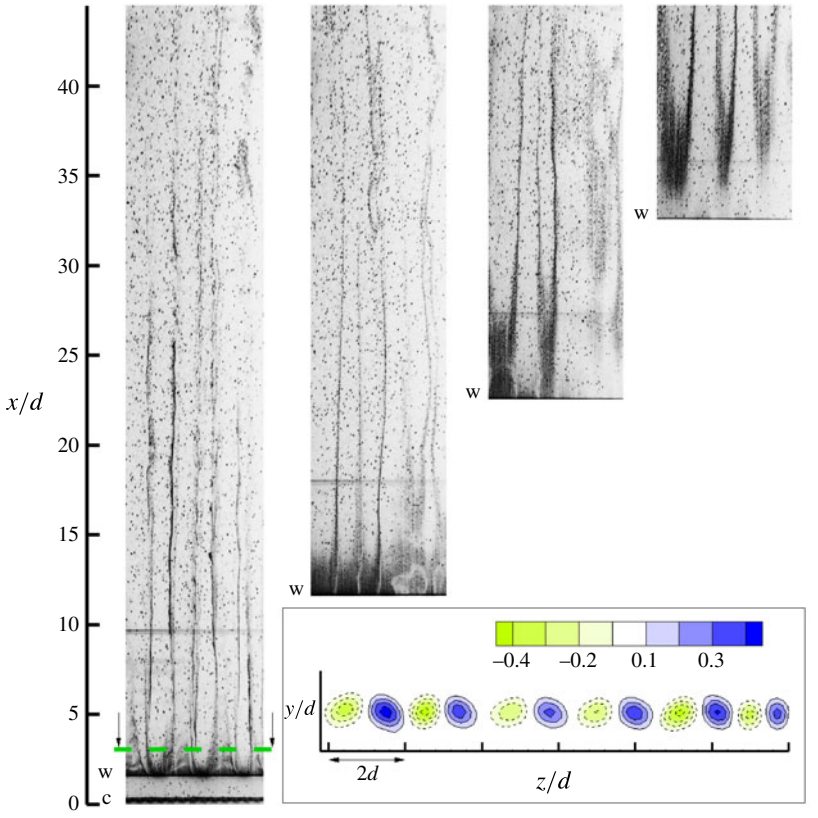

FIGURE 12. (Colour online) Inverse colour photographs of streakline patterns of mode E when the hydrogen bubble wire is placed at increasing distances downstream of the cylinder ($Re = 250$, $\alpha = 2.1$). The location of the cylinder is marked with 'c', all wire positions are marked with 'w'. The insert on the lower right shows non-dimensional streamwise vorticity obtained from time-averaged PIV data in the y–z plane (the view is in upstream direction; vorticity is non-dimensionalized as $\omega_x d/U$; negative vorticity is denoted by broken lines and solid lines represent positive values). The PIV recording location is marked in the first photograph on the left with the dashed line (shown in green online) at $x/d = 3$.

An estimate of the strength of the streakline effect is given in figure 12 for mode E. Following Cimbala *et al.* (1988), the hydrogen bubble wire was placed at increasing distances downstream of the cylinder. The photographs show that the bubble sheet is deformed periodically along the span as far as $x/d > 30$, meaning that the streamwise vortices of mode E exist at least up to this distance. It can be concluded that the streakline effect plays a minor role in our visual data, and the photographs show a good estimate of the true location and strength of streamwise vorticity.

To support our flow visualizations and to confirm the spanwise periodicity of mode E, PIV data in the y–z plane at $x/d = 3$ were recorded. For this plane orientation, the streamwise vortices 'pierce' the laser plane almost perpendicularly and create a periodic in-plane fluid motion. The vortices were strictly stationary, such that a time average of 500 PIV snapshots (1 s apart) could be calculated. The insert on the lower right of figure 12 shows vorticity contours of this time-averaged vector field. Counter

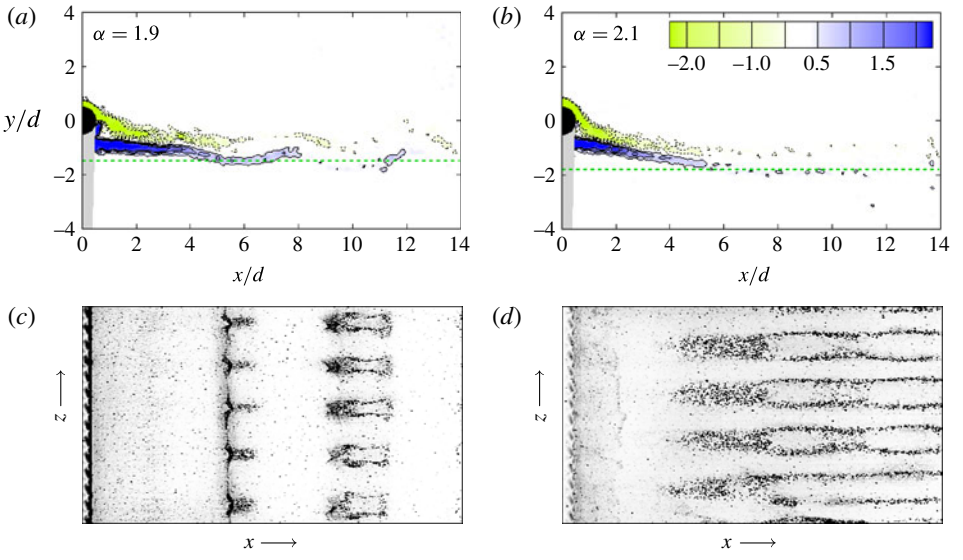

FIGURE 13. (Colour online) Comparing PIV and flow visualizations of modes D (*a,c*) and E (*b,d*) at $Re = 250$, $\alpha = 1.9$ and 2.1, respectively. The PIV data show the instantaneous vorticity fields in the *x*–*y* plane, and the flow visualizations are recorded from a side perspective in the *x*–*z* plane. The horizontal dashed lines in (*a*,*b*) show approximate locations of the laser sheet used to illuminate the hydrogen bubbles. The images have the same scale, but were not taken simultaneously. The colour maps have been inverted to better show the flow structures. (The flow is from left to right; vorticity is non-dimensionalized as $\omega_z d/U$.)

rotating vortex pairs can be clearly distinguished with a spanwise spacing of $2.05d$, confirming the visual data and the space–time diagram.

Returning to the comparison of modes D and E, it has been mentioned that the transition between these modes is dominated by the gradual decay of the main vortex shedding. This makes it difficult to determine a precise critical rotation rate separating these two modes. Considering the similar wavelengths and spatiotemporal symmetries, we speculate that these modes result from the same physical mechanism, but grow on different but related base flows. As shown by PIV data in § 3.2, shedding decayed for $Re = 200$ and rotation rates beyond $\alpha = 1.9$. As the critical rotation rate of this process is only weakly dependent on Reynolds number, the wake can be expected to undergo transition back to steady flow at a rotation rate in the range $1.9 < \alpha < 2$, even for Reynolds numbers above 200. This would explain the striking similarity between modes D and E.

We wanted to confirm this process at $Re = 275$, and link the flow fields in the wake cross-section (*x*–*y* plane) to visual observations from a side perspective. Figure 13 shows instantaneous PIV vorticity fields in the *x*–*y* plane, and flow visualizations in the *x*–*z* plane. As expected, the PIV data confirm the shedding decay in the range $1.9 < \alpha < 2.1$. Flow visualizations of the shedding wake show mode D structures, periodic in the spanwise and streamwise direction (figure 13*c*). Once the wake becomes steady, the spanwise periodicity persists, as seen in figure 13(*d*), whereas the structures now resemble streamwise vortices in a plane parallel to the *x*–*z* plane (mode E).

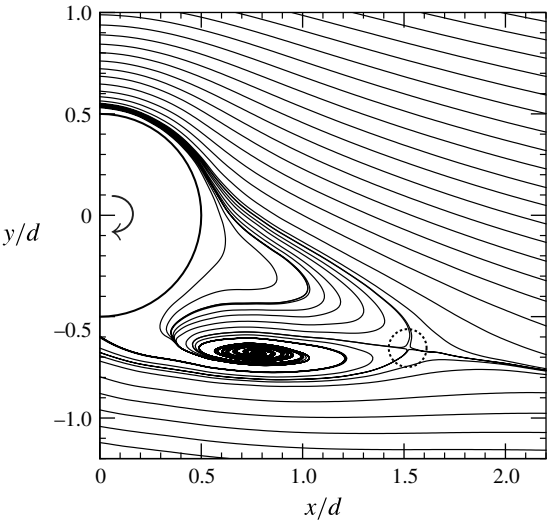

FIGURE 14. Time-averaged streamlines (PIV data) at $Re = 250$ showing the location of the hyperbolic point (dashed circle) in the wake of the cylinder rotating at $\alpha = 1.90$. The approximate coordinates of this point are $(x, y) = (1.52d, -0.66d)$. The flow is from left to right.

The approximate location of the laser sheet, which creates these flow visualizations, is indicated in the PIV vorticity fields as a dashed line. The cut through the serpentine wake at $\alpha = 1.9$ creates the interrupted patterns seen in figure 13(*c*), whereas the cut through the steady wake at $\alpha = 2.1$ appears in figure 13(*d*) as steady streamwise structures.

The PIV data of figure 13 give clues on the physical mechanism behind these two modes. Up to $x/d \approx 4$, the wakes of both modes are practically identical, consisting of a steady double-shear layer. Only further downstream, the wake develops an oscillation for $\alpha = 1.9$. An enlarged view of the time-averaged near-wake for $Re = 250$ and $\alpha = 1.90$ is shown in figure 14. The two prominent features of this flow field are a single closed recirculation region (rather a focal point), and a hyperbolic point at $(x, y) = (1.52d, -0.66d)$. The flow field of mode E at $\alpha = 2.10$ is not shown, but displays the same characteristics, with the hyperbolic point moved slightly upstream to $(x, y) = (1.19d, -0.68d)$.

The hyperbolic stagnation point is characterized by local acceleration of fluid and rapid stretching of vortices, resulting in amplification of vorticity perturbations. As shown by Kerr & Dold (1994) and Leblanc & Godeferd (1999), hyperbolic instability can lead to formation of counter-rotating vortices ('ribs'), whose axes lie parallel to the direction of the diverging flow. This mechanism has been proposed by Williamson (1996*b*) and Leweke & Williamson (1998*b*) as reason for mode B in the wake of a stationary cylinder. (For an alternative viewpoint on the nature of mode B, see Ryan, Thompson & Hourigan (2005).) They argued that mode B scales on the smaller dimensions of the braid shear layer, which explains its comparable small wavelength of $1d$. In the case of mode D and E, the maximum streamwise vorticity occurs on the dividing streamline passing through the hyperbolic point, consistent with this hypothesis. Further discussion on this point can be found in Rao *et al.* (2013*a*).

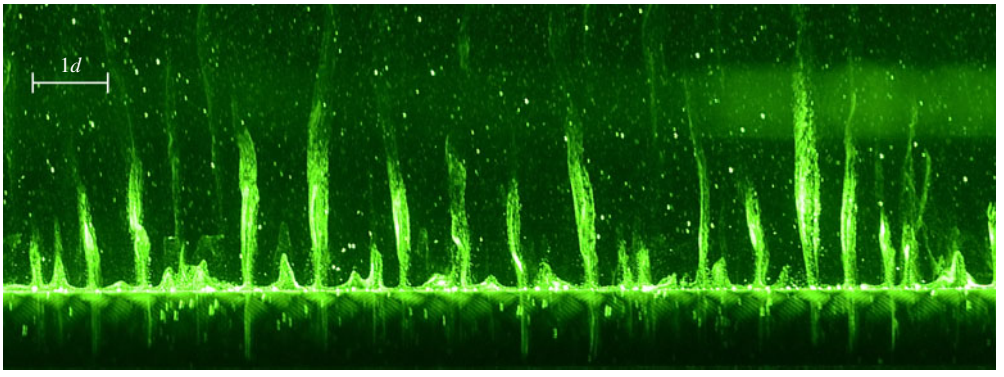

FIGURE 15. (Colour online) Flow visualization of mode F on the surface of the spinning cylinder, at $Re = 275$ and $\alpha = 2.3$. The average spanwise wavelength is $\lambda_z/d \approx 0.5$. The flow is from bottom up. The sense of rotation is such that the cylinder surface seen by the observer is moving up.

4.4. *Mode F*

The last instability investigated was the short-wavelength mode F, appearing at rotation rates above $\alpha \approx 2.2$, at $Re = 275$. Its flow structures formed on the cylinder surface, with an average spanwise spacing of $\lambda_z/d \approx 0.5$. These structures consisted of streamwise vortex filaments, partly wrapping around the cylinder and extending into the near wake, as seen in the flow visualization in figure 15. Considering the relatively high rotation rates and small length scales, a centrifugal instability seems to be the most likely explanation for this mode. Similar structures have been observed in the three-dimensional computations by Mittal (2004) at $Re = 200$ and $\alpha = 5$, and were linked to the centrifugal instability mechanism. Further analysis of this proposed mechanism to this case can be found in Rao *et al.* (2013*a*).

Unlike the previously discussed modes of this study, the streamwise vortices of mode F were not stationary, but wandered along the cylinder span. This can be seen in the space–time diagram of figure 16 (created at $x/d = 1$), which shows a consistent pattern of almost parallel inclined lines. These are oriented along the direction bottom left to top right, and are intersected by another group, orientated along bottom right to top left. A two-dimensional autocorrelation of the full space–time diagram (only a 15 s segment is shown here) displays two correlation maxima in directions indicated by the two white lines. The inverse slopes of these lines are the average phase velocities $\pm c_{ph}$ (in units of cylinder diameters per second) of mode F structures moving in positive and negative spanwise directions. Estimations of frequency ($f = c_{ph}/\lambda_z$) and spanwise Strouhal number ($St_{3D} = fd/U$) of this mode are shown in table 2. The three-dimensional Strouhal number is in good agreement with predictions by Rao *et al.* (2013*a*) (0.11).

These results suggest that mode F is a travelling wave. Rao *et al.* (2013*a*) reported a change in sign of streamwise vorticity within one perturbation field period. After a half period, the perturbation field was identical but of opposite sign. It was speculated that mode F is subharmonic, although the present experimental results support the travelling wave explanation.

Furthermore, there are signs of coexistence and nonlinear interaction of modes E and F. This is evident from the parameter space in figure 1, which shows an overlap region of these two modes for $Re > 290$ and $\alpha \geqslant 2.2$. Our experiments confirm the

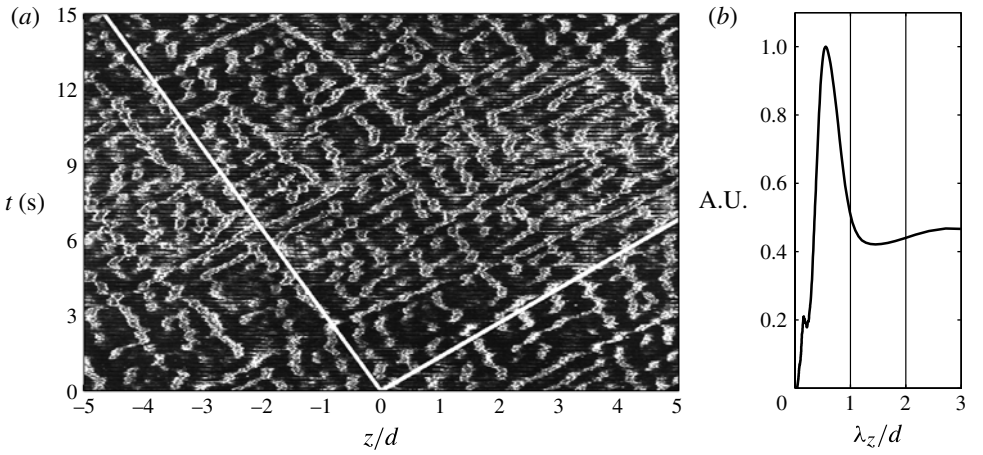

FIGURE 16. (*a*) Space–time diagram and (*b*) time-averaged wavelength spectrum of mode F at $Re = 275$, $\alpha = 2.3$. White lines in (*a*) show principal directions of movement of mode F structures.

	$-z$ direction	$+z$ direction	Mean
Phase velocity (d/s)	0.42	0.52	0.47
Frequency (Hz)	0.76	0.95	0.85
St_{3D}	0.09	0.11	0.10

TABLE 2. Characteristics of spanwise movement of mode F.

existence of structures similar to mode E in the far wake, even at slightly lower Reynolds numbers. Figure 17 shows the cylinder wake at $Re = 275$ and $\alpha = 2.4$ (for better clarity and contrast, the wire is positioned downstream of the cylinder). There is a striking visual similarity to mode E of figure 10(*b*). The dominant spanwise wavelength at this rotation rate lies between 1.6 and 2 cylinder diameters, compared with $\lambda_z/d \approx 2.1$ of the 'pure' mode E.

Despite the visual similarity, two characteristics distinguish this flow regime from mode E: first, the streamwise structures visible in figure 17 are moving in the spanwise direction. Numerical processing shows that the phase velocity is $c_{ph} \approx \pm 0.5$ d/s, similar to that of mode F. This is the first sign of a possible interaction between these two modes. The second difference is the appearance of 'loop-like' structures in the far wake, some of which are marked by dashed circles. This phenomenon has not been observed in the case of pure mode E. Preliminary experiments indicate that these structures are created in the vicinity of the cylinder by ejection of large hairpin vortices (of the order of $2d$) into the near wake. Nevertheless, the physics involved is not clear at this stage and should be investigated in future work.

4.5. *Second shedding*

Although outside the main scope of this paper, we would like to add a short note on the subject of second shedding, as reported by Mittal & Kumar (2003), Stojković *et al.* (2003), El Akoury *et al.* (2008) and Kumar *et al.* (2011). It is remarkable

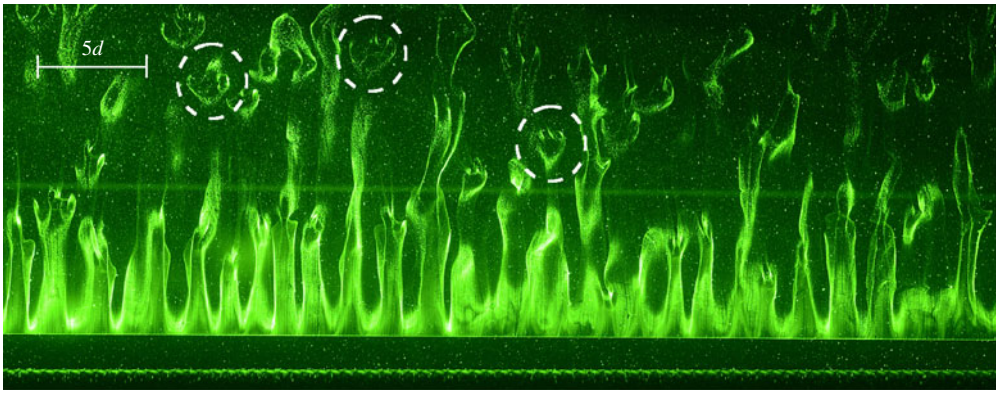

FIGURE 17. (Colour online) Flow visualization at $Re = 275$ and $\alpha = 2.4$, showing streamwise structures similar to mode E. Not visible in this picture, due to the chosen hydrogen bubble location, is mode F on the surface of the cylinder, similar to figure 15. Dashed circles mark 'loop-like' structures that distinguish this flow regime from the pure mode E. The flow is from the bottom up.

that all evidence of this phenomenon presented in these publications are either two-dimensional computations, or experimental data (PIV and flow visualizations) of the wake cross-section. Stunningly, some studies report the absence of this phenomenon altogether (Luo *et al.* 2009). To our best knowledge, no published data exist that show this process in three dimensions. Without such data, the question arises how strictly two-dimensional this process is in reality. In other words, it is not clear whether the one-sided vortex detaches simultaneously along the whole cylinder span, or whether it happens as a three-dimensional process. In addition, recent numerical investigations by Rao *et al.* (2013*b*) showed the onset of the mode E instability prior to the onset of mode II shedding.

Initially, we hoped to observe this phenomenon under conditions reported by other researchers. For example, Kumar *et al.* (2011) presented instantaneous PIV vorticity maps in the wake cross-section at $Re = 200$ and $\alpha = 4.45$ that showed the detachment of a one-sided vortex from the rotating cylinder. For these conditions, we did not observe anything comparable in our flow visualizations. The near wake was in a permanent chaotic state. In addition, a centrifugal instability (mode F) was present on the cylinder surface, adding to the disruption of the near wake. This is consistent with observations by Mittal (2004), who reports small structures along the span of the cylinder. Nevertheless, large-scale vortical structures could be observed being ejected at random intervals into the wake in our experiment, containing large amounts of vorticity. This process can be seen in the online supplementary movie 'Movie2.mp4' accompanying this article (available at http://dx.doi.org/10.1017/jfm.2012.486).

The closest phenomenon resembling second shedding was observed only when we significantly reduced the Reynolds number. This had two effects: the wake became more stable; and the centrifugal instability was suppressed due to the lower rotation rates. In this 'clean' wake, we made the observation of a single-sided vortex detachment at $Re = 100$ and $\alpha = 5.1$. Against expectations, this process was very localized, initiating from random 'detachment points' along the cylinder span in an unpredictable fashion.

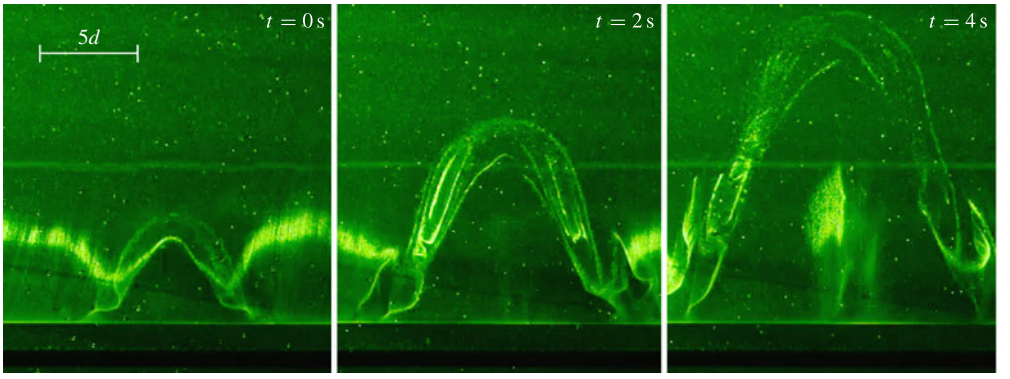

FIGURE 18. (Colour online) Flow visualization of one-sided shedding at $Re = 100$ and $\alpha = 5.1$ (video snapshots taken from the first few seconds of 'Movie3.mp4'). The detaching vortex forms a horse-shoe shaped vortex bend, which peels slowly off the cylinder. The rotating cylinder can be seen at the bottom edge; the hydrogen bubble wire is positioned downstream of it. The flow is from the bottom up. The contrast has been enhanced for clarity.

Figure 18 shows three video snapshots cropped around one of these points. The overall wake is initially steady. The first picture shows the start of detachment, as the vortex passes the hydrogen bubble wire. The vortex wraps the bubble sheet into a horse-shoe shaped tube. As this peeling process continues, the base of the 'horse-shoe' structure widens, its two end points moving apart in the spanwise direction. In most cases, the process stops only when one of these base points reaches the base point of a neighbouring vortex bend. The full detachment sequence of this, and several other vortex bends, can be seen in supplementary movie 'Movie3.mp4'.

No further data were collected on this phenomenon, and at this point it can only be speculated on the reasons for the described behaviour. Is the observed three-dimensionality due to end effects of the finite cylinder, the imperfections of the experimental setup (free-stream turbulence and unavoidable (but small) cylinder vibrations), or is this process inherently three-dimensional? Previously published observations in the cross-sectional plane might be the result of an opportune positioning of the recording plane. A cut parallel and close to the symmetry plane of one of these vortex bends would appear in planar PIV vector fields as a single spanwise vortex moving downstream.

On the other hand, PIV recordings by Kumar *et al.* (2011) confirm one-sided shedding at $Re = 200$, a Reynolds number at which no coherent shedding was visually perceivable in our experiments. One explanation for this might be the interaction of centrifugal instability and second shedding. One-sided shedding may be present in our flow, but visually masked by the flow disruptions caused by centrifugal instability. The previously mentioned ejection of large-scale vortical structures at this Reynolds number might in fact consist of actual vortex bends, disrupted and deformed by the interaction with mode F. For now, these claims are of a speculative nature and further thorough investigation is needed to address these issues.

5. Conclusions

The results presented here are the first to show experimentally a new set of three-dimensional modes in the wake of a rotating cylinder. These match the modes first found in the numerical work based on linear stability analysis of Rao *et al.* (2013*a*).

First, the experimental setup was validated for cases of a non-spinning and a spinning cylinder. Modes A and B were observed in the wake of a non-spinning cylinder at $Re = 175$ and 275, respectively. In the case of a rotating cylinder, PIV results by Kumar *et al.* (2011) were reproduced for $Re = 200$. Shedding decayed once the rotation rate passed the critical value of $\alpha \approx 1.9$, and the wake developed into a steady double-shear layer.

During the main experiments, several new three-dimensional modes were investigated for Reynolds numbers 250 and 275. First, a subharmonic mode C was observed for rotation rates $1.0 \lesssim \alpha \leqslant 1.85$. Its nominal spanwise wavelength was $\lambda_z/d \approx 1.1$ at $\alpha = 1.7$, but increased significantly with decreasing rotation rate. This mode has similar characteristics to the subharmonic mode C observed in the wakes of a torus (Sheard *et al.* 2005*a*), and of a cylinder disturbed by a thin wire (Zhang *et al.* 1995; Yildirim *et al.* 2013). Furthermore, a complex interaction with mode B took place for $\alpha \lesssim 1.0$. This nonlinear interaction could not be predicted by linear stability analysis.

Two modes with a wavelength of $\lambda_z/d \approx 2$ appeared in close succession at $Re = 250$. For rotation rates above $\alpha = 1.85$, mode D consisted of continuous streamwise vortices in a shedding wake. Mode E was observed at a slightly higher rotation rate of $\alpha \geqslant 2.1$. It appears that this mode is a continuation of mode D, but on a henceforth steady wake. This is supported by the observation of a smooth transition between these two modes, as the wake changes gradually from a shedding to a steady state. Both modes are attributed to an hyperbolic instability of the mean wake.

The fourth mode, mode F, was observed on the cylinder surface for $Re = 275$ and rotation rates above $\alpha \approx 2.2$. It consisted of ring-like vortices at an average spanwise spacing of $\lambda_z/d \approx 0.5$. Similar structures with a spanwise wavelength of one cylinder diameter were observed in three-dimensional computations by Mittal (2004) for $\alpha = 5$. It is speculated that this mode is the result of centrifugal instability. However, in our experiments, the three-dimensional structures moved along the span, resembling a travelling wave of $St_{3D} \approx 0.1$. In addition, while mode F was fully developed on the cylinder surface, streamwise structures similar to mode E were observed in the wake for rotation rates $\alpha \geqslant 2.3$. There is indication of a nonlinear interaction between these two modes that needs further investigation.

One-sided shedding (second shedding mode) was visualized for $Re = 100$, $\alpha = 5.1$ (see supplementary movie 'Movie3.mp4'). Unlike the current assumption of a two-dimensional vortex parallel to the cylinder axis, the observed shedding created localized horse-shoe shaped vortex structures peeling off the cylinder. The detachment was initiated at randomly distributed 'detachment points' along the span, giving this process a fully three-dimensional character.

In summary, the presented experimental results largely confirm the linear stability analysis of Rao *et al.* (2013*a*). The predicted modes C–F have been observed experimentally, with a good agreement in terms of spanwise wavelengths and spatiotemporal symmetries. All modes are shown in sequence at $Re = 275$ in the supplementary movie 'Movie1.mp4', which can be found online.

The largest discrepancy concerns the observation of mode C at rotation rates significantly below its linearly unstable range. A possible cause might be the fully developed mode B as the initial condition in the experiment. This does not seem to play a role for $\alpha > 1.0$, but leads to a complex interaction of these two modes for $\alpha \lesssim 1.0$, which should be investigated in future work.

Acknowledgements

The authors appreciate the support of Dr D. Lo Jacono for assistance with the data processing. The project was supported by an Australian Research Council (grant number DP130100822). A. Rao acknowledges financial support of a Monash University Postgraduate Publication Award.

Supplementary movies

Supplementary movies are available at http://dx.doi.org/10.1017/jfm.2013.486.

REFERENCES

BARKLEY, D. & HENDERSON, R. D. 1996 Three-dimensional Floquet stability analysis of the wake of a circular cylinder. *J. Fluid Mech.* **322**, 215–241.

BARKLEY, D., TUCKERMAN, L. S. & GOLUBITSKY, M. 2000 Bifurcation theory for three-dimensional flow in the wake of a circular cylinder. *Phys. Rev.* E **61** (5), 5247–5252.

BÉNARD, H. 1908 Formation de centres de giration à l'arriere d'un obstacle en mouvement. *C. R. Acad. Sci. Paris* **147**, 839–842.

BLACKBURN, H. M. & LOPEZ, J. M. 2003 On three-dimensional quasi-periodic Floquet instabilities of two-dimensional bluff body wakes. *Phys. Fluids* **15**, L57–L60.

CIMBALA, J., NAGIB, H. & ROSHKO, A. 1988 Large structure in the far wakes of two-dimensional bluff bodies. *J. Fluid Mech.* **190**, 265–298.

DÉLERY, J. M. 2001 Robert Legendre and Henri Werlé: toward the elucidation of three-dimensional separation. *Annu. Rev. Fluid Mech.* **33** (1), 129–154.

DUSEK, J., LE GAL, P. & FRAUNIE, D. P. 1994 A numerical and theoretical study of the first Hopf bifurcation in a cylinder wake. *J. Fluid Mech.* **264**, 59–80.

EL AKOURY, R., BRAZA, M., PERRIN, R., HARRAN, G. & HOARAU, Y. 2008 The three-dimensional transition in the flow around a rotating cylinder. *J. Fluid Mech.* **607**, 1–11.

FOURAS, A., LO JACONO, D. & HOURIGAN, K. 2008 Target-free stereo PIV: a novel technique with inherent error estimation and improved accuracy. *Exp. Fluids* **44** (2), 317–329.

HENDERSON, R. 1997 Nonlinear dynamics and pattern formation in turbulent wake transition. *J. Fluid Mech.* **352**, 65–112.

JACKSON, C. P. 1987 A finite-element study of the onset of vortex shedding in flow past variously shaped bodies. *J. Fluid Mech.* **182**, 23–45.

KÁRMÁN, TH. VON 1911 Über den Mechanismus des Widerstandes, den ein bewegter Körper in einer Flüsseigkeit erfährt. *Gött. Nachr* **5**, 509–517.

KERR, O. S. & DOLD, J. W. 1994 Periodic steady vortices in a stagnation-point flow. *J. Fluid Mech.* **276**, 307–325.

KUMAR, B. & MITTAL, S. 2006 Effect of blockage on critical parameters for flow past a circular cylinder. *Intl J. Numer. Meth. Fluids* **50** (8), 987–1001.

KUMAR, S, CANTU, C. & GONZALEZ, B. 2011 Flow past a rotating cylinder at low and high rotation rates. *J. Fluids Engng* **133** (4), 041201.

LE GAL, P., NADIM, A. & THOMPSON, M. C. 2001 Hysteresis in the forced Stuart–Landau equation: application to vortex shedding from an oscillating cylinder. *J. Fluids Struct.* **15**, 445–457.

LEBLANC, S. & GODEFERD, F. S. 1999 An illustration of the link between ribs and hyperbolic instability. *Phys. Fluids* **11** (2), 497–499.

LEWEKE, T. & WILLIAMSON, C. H. K. 1998*a* Cooperative elliptic instability of a vortex pair. *J. Fluid Mech.* **360**, 85–119.

LEWEKE, T. & WILLIAMSON, C. H. K. 1998*b* Three-dimensional instabilities in wake transition. *Eur. J. Mech. (*B*/Fluids)* **17**, 571–586.

LUO, S. C., CHEW, Y. T. & DUONG, T. T. L. 2009 PIV investigation of flow past a rotating circular cylinder. In *Fourth International Conference on Experimental Mechanics*, Proc. SPIE, vol. 7522, International Society for Optics and Photonics, article 752219.

MILLER, G. D. & WILLIAMSON, C. H. K. 1994 Control of three-dimensional phase dynamics in a cylinder wake. *Exp. Fluids* **18** (1), 26–35.

MITTAL, S. 2001 Flow past rotating cylinders: effect of eccentricity. *Trans. ASME: J. Appl. Mech.* **68** (4), 543–552.

MITTAL, S. 2004 Three-dimensional instabilities in flow past a rotating cylinder. *Trans. ASME: J. Appl. Mech.* **71** (1), 89–96.

MITTAL, S. & KUMAR, B. 2003 Flow past a rotating cylinder. *J. Fluid Mech.* **476**, 303–334.

NORBERG, C. 1987 Effect of Reynolds number and a low-intensity free stream turbulence on the flow around a circular cylinder. PhD thesis, Chalmers University of Technology, Gothenburg, Sweden.

PRALITS, J., BRANDT, L. & GIANNETTI, F. 2010 Instability and sensitivity of the flow around a rotating circular cylinder. *J. Fluid Mech.* **650**, 513–536.

PRALITS, J. O., GIANNETTI, F. & BRANDT, L. 2013 Three-dimensional instability of the flow around a rotating circular cylinder. *J. Fluid Mech.* **730**, 5–18.

PRASAD, A. & WILLIAMSON, C. H. K. 1997 Three-dimensional effects in turbulent bluff-body wakes. *J. Fluid Mech.* **343**, 235–265.

RAO, A., LEONTINI, J., THOMPSON, M. C. & HOURIGAN, K. 2013*a* Three-dimensionality in the wake of a rotating cylinder in a uniform flow. *J. Fluid Mech.* **717**, 1–29.

RAO, A., LEONTINI, J. S., THOMPSON, M. C. & HOURIGAN, K. 2013*b* Three-dimensionality in the wake of a rapidly rotating cylinder in uniform flow. *J. Fluid Mech.* **730**, 379–391.

RYAN, K., THOMPSON, M. C. & HOURIGAN, K. 2005 Three-dimensional transition in the wake of elongated bluff bodies. *J. Fluid Mech.* **538**, 1–29.

SHEARD, G. J., THOMPSON, M. C. & HOURIGAN, K. 2003*a* A coupled Landau model describing the Strouhal–Reynolds number profile of the three-dimensional wake of a circular cylinder. *Phys. Fluids* **15** (9), L68–L71.

SHEARD, G. J., THOMPSON, M. C. & HOURIGAN, K. 2003*b* From spheres to circular cylinders: the stability and flow structures of bluff ring wakes. *J. Fluid Mech.* **492**, 147–180.

SHEARD, G. J., THOMPSON, M. C. & HOURIGAN, K. 2005*a* The subharmonic mechanism of the mode C instability. *Phys. Fluids* **17** (11), 111702.

SHEARD, G. J., THOMPSON, M. C., HOURIGAN, K. & LEWEKE, T. 2005*b* The evolution of a subharmonic mode in a vortex street. *J. Fluid Mech.* **534**, 23–38.

SMITS, A. J. & LIM, T. T. 2000 *Flow Visualization: Techniques and Examples*, 1st edn. Imperial College Press.

STOJKOVIĆ, D., SCHÖN, P., BREUER, M. & DURST, F. 2003 On the new vortex shedding mode past a rotating circular cylinder. *Phys. Fluids* **15**, 1257–1260.

THOMPSON, M., HOURIGAN, K. & SHERIDAN, J. 1996 Three-dimensional instabilities in the wake of a circular cylinder. *Exp. Therm. Fluid Sci.* **12** (2), 190–196.

THOMPSON, M. C., LEWEKE, T. & WILLIAMSON, C. H. K. 2001 The physical mechanism of transition in bluff body wakes. *J. Fluids Struct.* **15**, 607–616.

WILLIAMSON, C. H. K. 1988 The existence of two stages in the transition to three-dimensionality of a cylinder wake. *Phys. Fluids* **31** (11), 3165–3168.

WILLIAMSON, C. H. K. 1992 The natural and forced formation of spot-like 'vortex dislocations' in the transition of a wake. *J. Fluid Mech.* **243**, 393–441.

WILLIAMSON, C. H. K. 1996*a* Mode A secondary instability in wake transition. *Phys. Fluids* **8** (6), 1680–1682.

WILLIAMSON, C. H. K. 1996*b* Three-dimensional wake transition. *J. Fluid Mech.* **328**, 345–407.

WILLIAMSON, C. H. K. 1996*c* Vortex dynamics in the cylinder wake. *Annu. Rev. Fluid Mech.* **28** (1), 477–539.

WU, J., SHERIDAN, J., WELSH, M. C. & HOURIGAN, K. 1996 Three-dimensional vortex structures in a cylinder wake. *J. Fluid Mech.* **312**, 201–222.

YILDIRIM, I., RINDT, C. C. M. & VAN STEENHOVEN, A. A. 2010 Vortex dynamics in a wire-disturbed cylinder wake. *Phys. Fluids* **22** (9), 094101.

YILDIRIM, I., RINDT, C. C. M. & VAN STEENHOVEN, A. A. 2013 Mode C flow transition behind a circular cylinder with a near-wake wire disturbance. *J. Fluid Mech.* **727**, 30–55.

ZHANG, H.-Q., FEY, U., NOACK, B., KÖNIG, M. & ECKELMANN, H. 1995 On the transition of the cylinder wake. *Phys. Fluids* **7** (4), 779–794.